Taylor & Francis
Taylor & Francis Group

A crystal plasticity finite element model for flow stress anomalies in Ni₃Al single crystals

Shahriyar Keshavarz[†] and Somnath Ghosh[*]

Department of Civil Engineering, Johns Hopkins University, Baltimore 21218, MD, USA

This paper presents a dislocation density-based non-Schmid constitutive model to address the anomalous thermo-mechanical behaviour of the $L1_2$ intermetallic single-crystal Ni₃Al. Ni₃Al is used as a strengthening precipitate (γ' phase) in Ni-based superalloys. Addressing such anomalous behaviour by accounting for temperature-dependent flow stress and hardening evolution, as well as orientation-dependent tension–compression asymmetry, is necessary for modelling superalloys across a range of temperatures. While hardening in cube-slip systems results from statistically stored dislocations (SSDs), hardening in octahedral slip systems is due to both SSDs and cross-slip dislocations (CSDs). The constitutive model incorporates hardening evolution due to SSDs and CSDs. Experimental data for Ni₃Al-type single crystals, available in the literature, are used to calibrate material parameters. Subsequently, results of crystal plasticity FEM simulations are compared with experimental data for several orientations under constant strain rate and creep loading conditions for a wide range of temperatures. The model is able to correctly predict the response of $L1_2$ intermetallic single crystals including features of anomalous flow stress and non-Schmid yield behaviour.

Keywords: intermetallic single crystals; anomalous flow stress; tension–compression asymmetry; cross-slip; non-Schmid yield

1. Introduction

Nickel-based superalloys are widely used in propulsion components of the aerospace industry such as turbine engine blades, disks, casings and liners. Large investments have been made in these alloys for improving strength, creep response and fatigue life properties with the notion of advancing the performance and life of these components in the field. To accomplish this, robust computational tools are needed for predicting the mechanical behaviour of these alloys with consequences in microstructural design. A majority of Nickel-based superalloys have a two-phase $\gamma-\gamma'$ microstructure as shown in Figure 1(a). The γ phase matrix (white) is a Nickel-rich FCC solid solution, while the γ' phase precipitate (black) is a coherent-ordered intermetallic phase Ni₃Al has a $L1_2$ crystal structure. The intermetallic γ' phase is a strengthening precipitate that provides superior thermomechanical properties to the overall superalloy. It appears as a distribution of nearly spheroidal or cuboidal precipitates embedded in the disordered

---
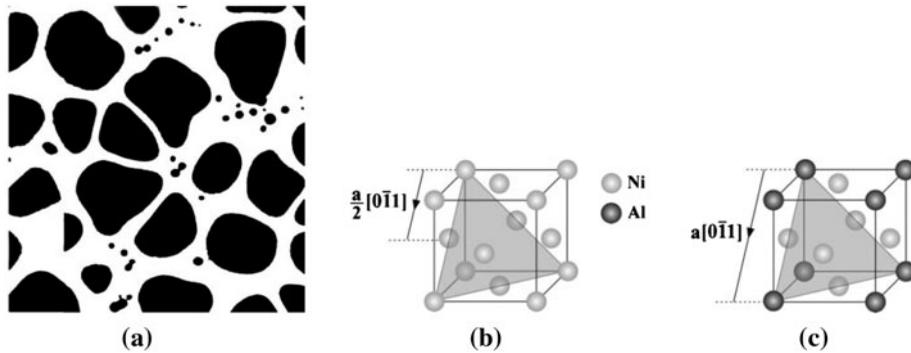
Figure 1. Microstructure of Ni-based superalloys: (a) two-phase $\gamma - \gamma'$ sub-grain microstructure of Rene 88-DT, (b) unit lattice structure of γ phase and (c) unit lattice structure of γ' phase.

Ni–Cr solid solution. The unit lattice structures of these two phases are shown in Figure 1(b) and (c). The solid solution Ni matrix has a regular FCC structure, while in a unit structure of the Ni_3Al crystal, the minority (Al) atoms occupy the corner sites and the majority (Ni) atoms occupy the face-centred sites. Mechanical properties of the Ni_3Al structured material are different from those of a regular FCC structured material. The main difference is the length of the Burgers vector for a full dislocation. The length of a full dislocation or superdislocation in $L1_2$ crystal is, $\langle 1\,1\,0 \rangle$ as opposed to $\frac{1}{2}\langle 110 \rangle$ for a full dislocation in regular FCC crystals.

The Ni_3Al-based $L1_2$ intermetallic γ' phase exhibits an anomalous dependence of the flow stress on temperature. This can be seen in the experimental data plots of Figures 8–12 for various experiments on a $Ni_3Al + 0.2\%B$ single crystal. Counter to the conventionally observed material behaviour of monotonic decrease of flow stress with increasing temperature, the flow stress for this alloy first increases with an increasing temperature to a peak value at a critical temperature of around 1000 K. Beyond this critical temperature, the flow stress drops rapidly with increasing temperature. At its peak, the flow stress is almost four times larger than its value at room temperature. This anomalous mechanical behaviour of Ni_3Al alloys is governed by a complex combination of underlying dislocation mechanisms. In the anomalous range (~below 1000 K), slip on octahedral slip systems dominates the deformation process as observed for various orientations and temperatures [1]. A significant fraction of the dislocations in this temperature range are immobile screw dislocations that lock in a Kear–Wilsdorf (KW) configuration as a result of cross-slip [2,3]. This phenomenon is demonstrated in Figure 3. There is general agreement in the literature that the predominant source of the anomalous yielding behaviour in Ni_3Al intermetallics is hardening caused by pinned segments of screw dislocations, when portions of $\langle 1\,1\,0 \rangle$ super-dislocations cross-slip from octahedral to cube planes. A secondary mechanism that is responsible for this behaviour is the activation of cube-slip systems. Cube planes are not closely packed planes in FCC materials and activation of cube-slip systems has been observed, especially at temperatures above the critical temperature of peak flow stress. Above this critical temperature, dislocations on cube planes are of both screw and edge dislocation types without any cross-slip.

Extensive research has been carried out to understand the underlying mechanisms causing anomalous temperature dependence of the flow stress. Early research on Ni_3Al-based $L1_2$ intermetallics focused on yield anomalies, while lately more attention is given to strain hardening and creep behaviour [4,5]. Takeuchi and Kuramoto [6] have studied temperature and orientation dependence of the flow stress in Ni_3 Ga single crystals based on a cross-slip pinning model. Lall et al. [1] have modified the model in [6] to include non-Schmid shear stresses as mechanisms responsible for the anomalous flow stress. Paidar et al. [7] have derived an enthalpy expression for the KW lock formation as a function of the resolved shear stresses on Shockley partials in primary and secondary slip planes. The core effects produced by the Shockley partials are responsible for tension–compression asymmetry and anti-phase boundary (APB) energy in octahedral and cubic planes. The enthalpy term in [7] has been used in several investigations for developing constitutive models including non-Schmid shear stresses. Cuitino and Ortiz [8] and Qin and Bassani [9] have used cross-slip activation enthalpy in the hardening parameters of rate-dependent constitutive models. Allan [10] has employed the same expression to determine the obstacle dislocation density due to cross-slip pinning. Kameda and Zikry [11] have proposed a constitutive model including mobile and immobile dislocation densities. Choi et al. [12] have developed a comprehensive constitutive model incorporating non-Schmid shear stresses to capture anomalous temperature dependence of the flow stress. While this behaviour is generally attributed to the structure of dislocations in the above models, most of them do not comprehensively address aspects of temperature dependence, crystal orientations, tension–compression asymmetry, offset strain criterion and cube-slip system activation in defining the response of single crystal Ni_3Al in a holistic crystal plasticity setting.

The aim of the present study is to develop a constitutive model incorporating non-Schmid shear stresses and APB shearing that can capture the temperature-dependent flow stress, strain hardening and creep behaviour of Ni_3Al single crystals. The APB shearing criterion enables manifestation of tension and compression asymmetry for different crystal orientations. This criterion is a function of (i) three non-Schmid shear stresses on the primary and secondary octahedral slip planes, and the cubic plane, (ii) the APB energy on octahedral and cubic planes and (iii) the temperature. In [20,21], the authors have developed a homogenized crystal plasticity constitutive model of Ni-based superalloys accounting for the subgrain scale $\gamma-\gamma'$ morphology in its constitutive parameters. The present work attempts to supplement the earlier papers with respect to the following aspects.

- Crystal plasticity constitutive modelling of single-phase Ni_3Al crystals is conducted, as opposed to superalloys in the earlier work.
- It covers a wide range of temperatures from room temperature to about 1000 °C, while the earlier work is in the vicinity of 800 °C only.
- The present work develops an orientation dependent constitutive model for Ni_3Al single crystals, whereas the earlier work was only for [0 0 1] orientation under tension loadings. The present work accounts for tension–compression asymmetry for a wide temperature range and all orientations.
- As opposed to hardening in Ni-based superalloys due statistically stored dislocations (SSDs) and geometrically necessary dislocations, hardening in Ni_3Al single crystals is due to SSDs and cross-slip dislocation densities (CSDs).

- The present work accounts for non-Schmid hardening in both primary and secondary octahedral slip systems, while the earlier work considered Schmid law for primary octahedral slip systems alone.
- Cube-slip systems are included as functions of the temperature in the present work, as experiments show they are operative especially at temperature greater than 800 °C.

Section 2 of this paper discusses some experimental observations for Ni_3Al single crystals at the macroscopic and microscopic scales. Section 3 develops a dislocation density-based crystal plasticity framework incorporating non-Schmid stresses and APB criterion as a function of cross-slip dislocation densities. Section 4 contains simulation results for both constant strain rate and creep tests. The paper concludes this development with a summary in Section 5.

2. Cross-slip mechanism and Kw lock formation

A super-dislocation in Ni_3Al often dissociates into superpartials, each having a Burgers vector $\frac{1}{2}\langle 1\,\bar{1}\,0\rangle$. When two superpartials separate, an APB is created. While APBs can form in both octahedral and cube planes, the cube plane APB energy is much lower than that for the octahedral planes. For a cube plane APB, the nearest-neighbour environment of the boundary atoms is the same as in the initial configuration, and differences occur only in the second and higher order neighbour distances [13]. This has been verified both analytically and experimentally with TEM measurements for stacking fault-type interfaces in [14,15]. For APB in the octahedral plane, the nearest-neighbour environment of the boundary atoms changes as shown in Figure 2, where three $(1\,1\,1)$ planes of Ni_3Al structure are stacked. The size of atoms decreases gradually from the top to the bottom planes. As shown in Figure 2(a), APB on the $(1\,1\,1)$ plane is facilitated by moving the top layer for $\frac{1}{2}[1\,\bar{1}\,0]$. The evolved atomic structure after the formation of APB is shown in Figure 2(b), where the nearest-neighbour environment of the boundary atoms is altered. Subsequently, each super-partial dislocation can dissociate into two Shockley partials, creating an interior complex stacking fault (CSF) as shown in Figure 2(a). In contrast to APB, the Shockley partials only dissociate on the octahedral planes [13,16]. The dissociation of $\langle 1\,\bar{1}\,0\rangle$ screw dislocations into two
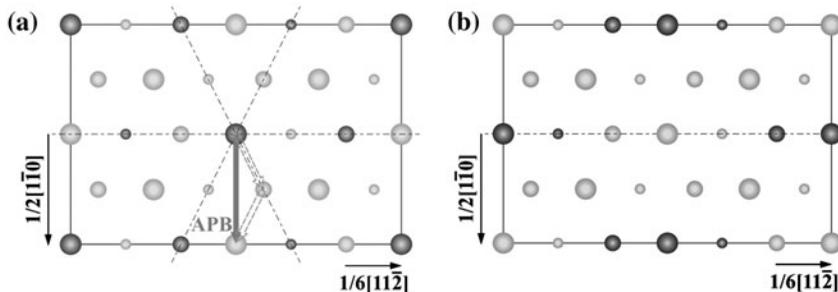
Figure 2. APB shearing and CSF mechanisms discussed in [13]: (a) before and (b) after shearing.

superpartials with a Burgers vector $\frac{1}{2}\langle 1\,\bar{1}\,0\rangle$ and consequently dissociation into Shockley partials has been widely observed. This is considered to have a major effect on the anomalous temperature dependence of flow stress in $L1_2$ single crystals. With increasing temperature, the screw dislocations tend to cross-slip from octahedral slip planes $\{1\,1\,1\}$ onto cube planes $\{0\,1\,0\}$ with drop in the APB energy. Subsequently, the cross-slipped dislocation drives back onto either a parallel $(1\,1\,1)$ or a non-parallel $(1\,\bar{1}\,1)$ octahedral plane. In the first case, the cross-slipped dislocation moves by a Burgers vector on the cube plane, while in the latter it moves by half a Burgers vector to create a non-planar KW lock [17] as shown in Figure 3. Due to the cross-slip of screw dislocations and formation of KW locks, the mobile dislocations become immobile, which results in the anomalous yield behaviour.

Experimental observations have confirmed that the cross-slip mechanisms in $L1_2$ single crystals do not conform to the Schmid's law commonly employed in crystal plasticity models [18]. In other words, Schmid's law breaks down in situations where the effect of partial dislocations comes to play or there are core effects. This law has been conventionally used to characterize the dependence of the resolved shear stress on
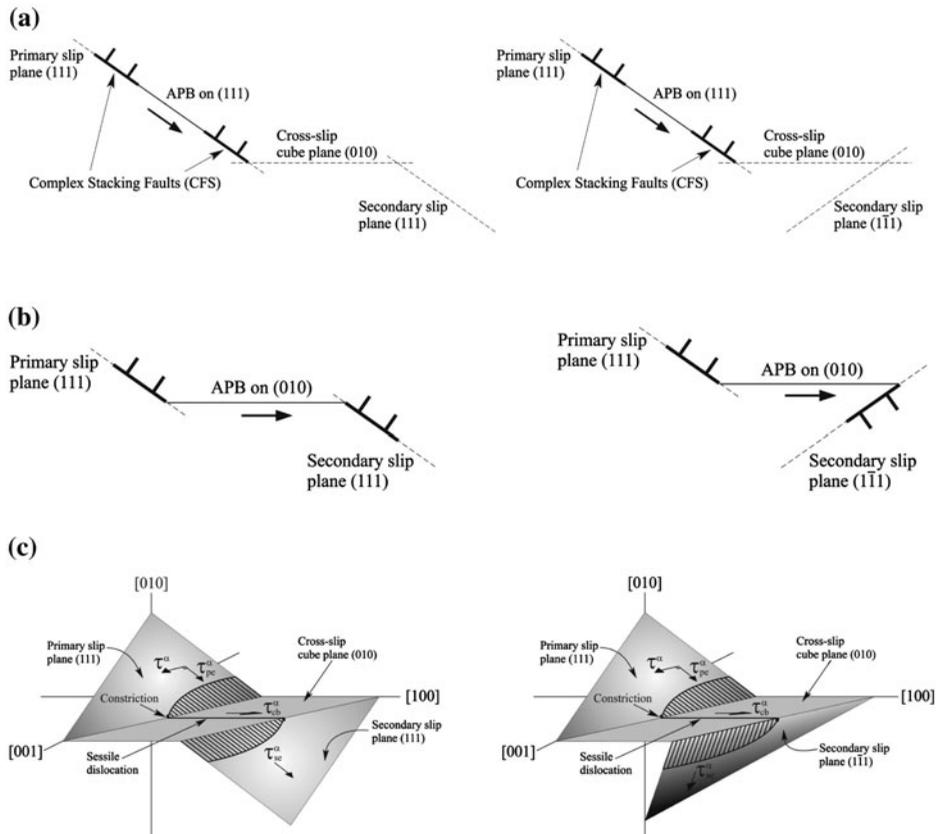
Figure 3. KW lock formation: (a) APB on the octahedral (primary slip) plane, (b) APB on the cube plane and (c) 3D configuration of KW lock.

loading orientation in the form of a simple geometric formula. The evolving hardness due to the cross-slip mechanism is asymmetric with respect to tension and compression loading and also depends on the crystal orientations. Contours of the maximum Schmid factor are plotted in n Figure 4(a), which shows the stereographic triangle having three orientations of $[0\,0\,1]$, $[0\,1\,1]$ and $[1\,1\,1]$ at the three corners. Experimental observations demonstrate that while the maximum Schmid factor for the two orientations $[0\,1\,0]$ and $[0\,1\,1]$ are similar, the corresponding flow stresses in tension and compression are different. The orientation $[1\,1\,1]$ with the least Schmid factor is expected to have maximum flow stress, but experiments show that this orientation will have the weakest flow stress as temperature rises. One of the reasons for the violation of Schmid's law is the activation of cube-slip systems. Cube-slip systems can be activated mainly for the grey area in Figure 4, which represents orientations with primary activation of cube-slip systems. In this region, the ratio of the Schmid factor for cube-slip systems is higher than that for the octahedral slip systems. Likewise, tension–compression asymmetry due to non-Schmid effects has been observed for almost all orientations. Orientations close to the $[0\,0\,1]$ on the stereographic triangle show a higher flow stress in tension while for orientations close to $[0\,1\,1]$, the compression flow stress is higher than the tensile strength.

TEM results e.g. in [17] show that in the temperature range of anomalies, the dislocations present are mostly long screw type as shown in Figure 5. These observations indicate that screw dislocations are much less mobile than edge dislocations and most of the dislocations responsible for the anomaly of increased flow stress are of the screw type. The sessile screw superdislocation segments are mostly locked in the KW configurations. Hence, $\{1\,1\,1\}\langle\bar{1}\,0\,1\rangle$ screw dislocations can cross-slip onto the cube planes, driven by a drop in APB energy. If the leading superpartials cross-slip onto a cube plane for some distance, then cross-slip back onto an octahedral plane and move forwards until the trailing superpartials meet the cross-slipped cube plane as shown in Figure 3. For geometrical reasons, individual Shockley partials do not cross-slip since $\frac{1}{6}\langle1\,1\,2\rangle$ lies only in the octahedral planes. According to Paidar et al. [7], once the partial dislocations become constricted as shown in Figure 3 and cross-slip, they move a short distance before they redissociate on $(1\,1\,1)$ plane. This plane can be either $(1\,1\,1)$ when the short distance is b, or $(1\,\bar{1}\,1)$ when the short distance is $\frac{b}{2}$. In Figure 3, there are three non-Schmid shear stresses participating in the creation of the KW lock. These are: (i) resolved shear stress τ_{pe}^{α} on the primary octahedral slip plane $(1\,1\,1)$, (ii) resolved shear stress τ_{cb}^{α} driving the dislocation in the cube plane after cross-slip and
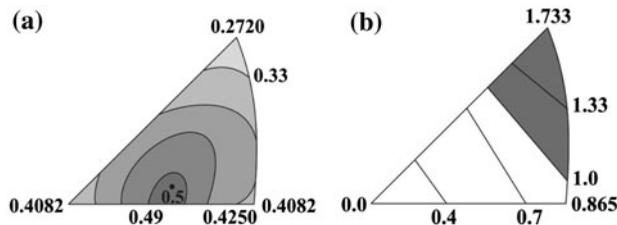
Figure 4. Contour plots of: (a) Schmid factor for octahedral slip system, and (b) ratio of Schmid factor of cube to octahedral slip systems in a stereographic unit triangle.
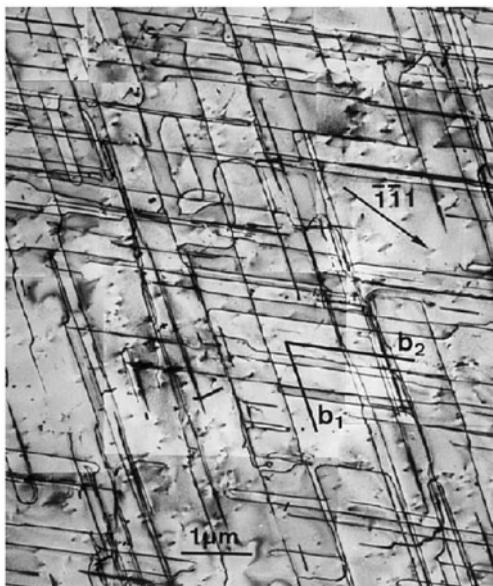
Figure 5. Dislocation structure of a Ni_3Al single-crystal compressed along the [0 0 1] direction at 600 °C. Long screw dislocation in KW configuration parallel to Burgers vectors b_1 and b_2 shown in [19]. (Reproduced with permission from Elsevier.)

(iii) resolved shear stress τ_{se}^{α} in either of the secondary (1 1 1) or $(1\,\bar{1}\,1)$ slip planes. As shown in Figure 4, the shear stress τ_{pe}^{α} constricts the Shockley partials and is partially responsible for the tension–compression asymmetry. For one of the load directions, τ_{pe}^{α} constricts the Shockley partials to promote cross-slip resulting in the higher flow stress, while in the opposite direction it hinders cross-slip with a decrease in flow stress.

3. Crystal plasticity constitutive model For Ni_3Al single crystals

Deformation of Ni_3Al involves the activation of 12 octahedral slip systems [10]. A commonly observed mechanism at a wide range of temperatures is that a super-dislocation dissociates into two superpartials each having a Burgers vector of $\frac{1}{2}\langle 1\,\bar{1}\,0\rangle$, creating a planar fault APB. Subsequently, the superpartials generally dissociate and split into two Shockley partials, bounding a CSF having Burgers vectors of $\frac{1}{6}\langle 1\,1\,2\rangle$. In order to incorporate the resolved shear stresses (τ_{pe}^{α}, τ_{se}^{α}) associated with the Shockley partials on primary and secondary octahedral planes, as shown in Figure 3, four octahedral slip planes corresponding to the {1 1 1} family, with three slip directions of the family $\langle 11\bar{2}\rangle$ for each of slip plane, are considered. On the other hand, thermally activated cross-slip mechanism results in τ_{cb}^{α} on cube planes, which is another non-Schmid component in the resolved shear stress.

3.1. *Activation of cube-slip systems*

Experimental observations indicate that below the peak temperature shown in Figure 6, dislocation glide on the primary octahedral plane {1 1 1} is responsible for plastic
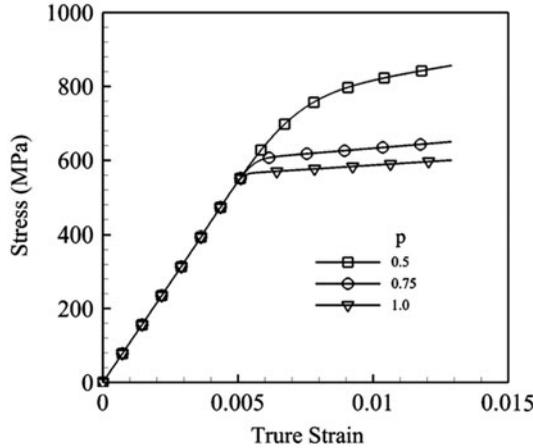
Figure 6. Sensitivity of the stress–strain response of Ni$_3$Al + 0.2%B single crystal to different values of exponent p in Equation (4).

deformation, while above this peak the primary cube plane $\{0\,0\,1\}$ controls the deformation process. However, this is not the case for orientations close to $[1\,1\,1]$ as discussed in [1]. For these orientations, traces of slip on cube-slip systems are observed at temperatures as low as 300 K, in addition to glide on the octahedral slip systems. To account for the resolved shear stress (τ_{cb}^{α}) due to cross-slip on the cube plane, as shown in Figure 3, six cube-slip planes of the $\{1\,0\,0\}$ family, each with two slip directions $\langle 0\,1\,\bar{1} \rangle$ are considered. Octahedral slip systems ($\alpha = 1-12$) and cube-slip systems ($\alpha = 13-18$), listed in Table 1, are considered for all temperature ranges. As seen in Figure 4(b), the Schmid factor for cube-slip systems for orientations near $[1\,1\,1]$ is higher than the Schmid factor for the octahedral slip systems. Note that immobilization of screw dislocations due to the KW locks, which results in anomalous increase in yield strength, occurs just for the octahedral slip systems. Hence, the APB shearing criterion differs for octahedral and cube orientations.

3.2. *Dislocation density-based crystal plasticity model*

Deformation in crystals results from a combination of elastic stretching, crystal lattice rotation and plastic slip on different lattice slip systems. Following developments in [21–24], large-strain kinematics in the crystal plasticity formulation is accommodated through a multiplicative decomposition of the total deformation gradient F into an

Table 1. Octahedral and cube-slip systems for Ni$_3$Al crystals.

α	1	2	3	4	5	6
$(n^{\alpha})[m^{\alpha}]$	$(1\,1\,1)[0\,\bar{1}\,1]$	$(1\,1\,1)[\bar{1}\,1\,0]$	$[\bar{1}\,1\,0][1\,0\,\bar{1}]$	$(1\,\bar{1}\,\bar{1})[1\,0\,1]$	$(1\,\bar{1}\,\bar{1})[0\,1\,\bar{1}]$	$(1\,\bar{1}\,\bar{1})[\bar{1}\,\bar{1}\,0]$
α	7	8	9	10	11	12
$(n^{\alpha})[m^{\alpha}]$	$(\bar{1}\,\bar{1}\,1)[\bar{1}\,0\,\bar{1}]$	$(\bar{1}\,\bar{1}\,1)[0\,1\,1]$	$(\bar{1}\,\bar{1}\,1)[1\,\bar{1}\,0]$	$(\bar{1}\,1\,\bar{1})[\bar{1}\,0\,1]$	$(\bar{1}\,1\,\bar{1})[0\,\bar{1}\,1]$	$(\bar{1}\,1\,\bar{1})[1\,1\,0]$
α	13	14	15	16	17	18
$(n^{\alpha})[m^{\alpha}]$	$(1\,0\,0)[0\,1\,1]$	$(1\,0\,0)[0\,1\,\bar{1}]$	$(0\,1\,0)[1\,0\,1]$	$(0\,1\,0)[1\,0\,\bar{1}]$	$(0\,0\,1)[1\,1\,0]$	$(0\,0\,1)[1\,\bar{1}\,0]$

incompressible inelastic component F^p associated with pure slip, and an elastic component F^e that accounts for elastic stretching and rigid-body rotations. This decomposition introduces an intermediate configuration that is free of plastic straining. A summary of the essential crystal plasticity equations are given below. The kinematic relations are:

$$F = F^e F^p, \quad \text{s.t.} \quad \det F^e > 1 \quad \text{and} \quad \det F^p = 1 \tag{1}$$

Evolution of plastic deformation is expressed in terms of the plastic velocity gradient L^p, the plastic shear rate $\dot{\gamma}^\alpha$ on slip system α, and Schmid tensor $s_0^\alpha \equiv m_0^\alpha \otimes n_0^\alpha$ (m_0^α and n_0^α are the slip direction and slip plane normal unit vectors in the reference configuration) as:

$$L^p = \dot{F}^p F^{-p} = \sum_{\alpha=1}^{N} \dot{\gamma}^\alpha m_0^\alpha \otimes n_0^\alpha = \sum_{\alpha=1}^{N} \dot{\gamma}^\alpha s_0^\alpha \tag{2}$$

The stress–strain relation is in terms of the second Piola–Kirchoff stress S and its work-conjugate the Lagrange–Green strain tensor E^e in the intermediate configuration that are expressed as:

$$S = det(F^e) F^{e-1} \sigma (F^{e-1})^T = C : E^e \text{ and } E^e \equiv \frac{1}{2}\{(F^e)^T F^e - F\} \tag{3}$$

Where I is the identity tensor, C is a fourth-order anisotropic elasticity tensor and σ is the Cauchy stress tensor. Ni_3Al exhibits plastic anisotropy, which is mostly accommodated through crystallographic slip on discrete slip systems and by the mechanism of APB formation. The signed dislocation density-based crystal plasticity model used for Nickel-based superalloys in [20,22,23] is modified in this work for rate-dependent plastic behavior Ni_3Al single crystals. These modifications are incorporated by adding cube-slip systems to the existing octahedral slip systems. On the other hand, the model incorporates the evolution of both SSDs due to four deformation mechanisms discussed in [20,22,23] and CSDs developed in this work. The plastic shearing rate on a slip system α is expressed using the Orowan equation:

$$\dot{\gamma}^\alpha = \rho_m^\alpha b v^\alpha, \quad \text{where} \quad v^\alpha = v_\circ \exp\left(-\frac{Q}{K_B \theta}\right) \sinh\left(\frac{|\tau^\alpha| - \tau_{\text{pass}}^\alpha}{\tau_{\text{cut}}^\alpha}\right)^p \text{sign}(\tau^\alpha) \tag{4}$$

Here ρ_m^α is the density of mobile dislocations, b is the Burgers vector and v^α is the velocity of dislocations on the slip system α. The velocity of dislocations is a function of the applied shear stress τ^α, the passing stress $\tau_{\text{pass}}^\alpha$ in the slip system and other slip system resistances. The term $v_\circ = \frac{c_1 \theta^{c_2}}{\sqrt{\rho_P^\alpha \rho_F^\alpha}}$ is the initial velocity, Q is the activation energy barrier, K_B is the Boltzmann's constant and θ K is the absolute temperature. An exponent p is incorporated in the argument of the sinh term in the present work for providing a control to the velocity for a given hardening evolution. Slip system resistances are represented in terms of (i) the passing stress $\tau_{\text{pass}}^\alpha$ due to the interaction of mobile dislocations with other dislocations and their networks in the slip plane and (ii) the cutting stress τ_{cut}^α due to the mobile dislocations cutting the forest dislocations with density ρ_F^α perpendicular to the slip plane. These stresses are expressed as [25]:

$$\tau_{\text{pass}}^{\alpha} = c_3 Gb \sqrt{\rho_P^{\alpha} + \rho_m^{\alpha}}, \quad \tau_{\text{cut}}^{\alpha} = \frac{c_4 K_{\text{B}} \theta}{b^2} \sqrt{\rho_F^{\alpha}} \tag{5}$$

where c_3 and c_4 are material constants and G is the shear modulus. Contributions to the overall slip resistance are assumed to be due to SSDs. The rate of evolution of statistically stored dislocation density denoted as $\dot{\rho}_{\text{SSD}}^{\alpha}$ has been identified in [25] as the net effect of components due to lock formation, dipole formation, athermal annihilation and thermal annihilation as:

$$\dot{\rho}_{\text{SSD}}^{\alpha} = \dot{\rho}_{\text{SSD}_{\text{lf}}}^{\alpha+} + \dot{\rho}_{\text{SSD}_{\text{df}}}^{\alpha+} + \dot{\rho}_{\text{SSD}_{\text{aa}}}^{\alpha-} + \dot{\rho}_{\text{SSD}_{\text{ta}}}^{\alpha-} \tag{6}$$

Superscripts $+/-$ correspond to multiplication and annihilation respectively. The rate increase due to lock formation, dipole formation and decrease due to mechanisms of dislocation annihilation due to thermal and athermal annihilation are respectively given as [25]:

$$\dot{\rho}_{\text{SSD}_{\text{lf}}}^{\alpha} = \frac{c_5}{b} \sqrt{\rho_F^{\alpha}} \, \dot{\gamma}^{\alpha}, \qquad \dot{\rho}_{\text{SSD}_{\text{df}}}^{\alpha} = \frac{c_6}{b} \frac{\sqrt{3}Gb}{16\pi(1-v)} \left(|\tau^{\alpha}| - \tau_{\text{pass}}^{\alpha} \right)^{-1} \rho_m^{\alpha} \dot{\gamma}^{\alpha},$$

$$\dot{\rho}_{\text{SSD}_{\text{aa}}}^{\alpha} = -c_7 \rho_{\text{SSD}}^{\alpha} \dot{\gamma}^{\alpha} \quad \text{and} \quad \dot{\rho}_{\text{SSD}_{\text{ta}}}^{\alpha} = -c_8 \frac{D_0 b^3}{k_B \theta} \exp\left(\frac{-Q_{\text{bulk}}}{k_B \theta}\right) \left(\rho_{\text{SSD}}^{\alpha}\right)^2 |\tau^{\alpha}| \left(\frac{\dot{\gamma}^{\alpha}}{\dot{\gamma}_{\text{ref}}}\right)^{c_9} \tag{7}$$

where c_5, c_6, c_7, c_8 and c_9 are material constants, D_0 is the diffusion co-efficient, Q_{bulk} is the activation energy for dislocation climb and $\dot{\gamma}_{\text{ref}}$ is a reference shear rate. Each of the contributing components in Equation (7) is a function of the slip rate $\dot{\gamma}^{\alpha}$, forest dislocation density, statistically stored dislocation density, component of applied shear stress τ^{α} and the absolute temperature θ. Thus, a general form is proposed as $\dot{\rho}_{\text{SSD}}^{\alpha} = \dot{\rho}_{\text{SSD}}^{\alpha}(\dot{\gamma}^{\alpha}, \rho_{\text{SSD}}^{\alpha}, \rho_F, \tau^{\alpha}, \theta)$. The forest and parallel dislocation densities are now written as functions of the SSDs [25] with an interaction strength coefficient $\chi\alpha\beta$ between different slip systems [26], as:

$$\rho_F^{\alpha} = \sum_{\beta=1}^{N} \chi^{\alpha\beta} \left[\rho_{\text{SSD}}^{\beta} \left| \cos\left(n^{\alpha}, t^{\beta}\right) \right| \right], \rho_P^{\alpha} = \sum_{\beta=1}^{N} \chi^{\alpha\beta} \left[\rho_{\text{SSD}}^{\beta} \left| \sin\left(n^{\alpha}, t^{\beta}\right) \right| \right] \tag{8}$$

This evolves with SSDs due to plastic deformation and hardening mechanisms. The density of mobile dislocations ρ_m^{α} is computed as a function of forest and parallel dislocation density and the temperature as:

$$\rho_m^{\alpha} = \frac{c_{10} k_B \theta \sqrt{\rho_F^{\alpha} \rho_P^{\alpha}}}{Gb^3} \tag{9}$$

3.3. Hardening related to thermally activated cross-slip mechanism

The CSDs act as local obstacles to further dislocation motion. The rate of generation of these obstacles is assumed to be proportional to the rate of cross-slip. The activation enthalpy for cross-slip depends on the APB energy on the primary octahedral slip and cube-slip planes, as well as on the non-Schmid components of the resolved shear stress. The non-Schmid shear stresses $\tau_{\text{pe}}^{\alpha}, \tau_{\text{se}}^{\alpha}$ and $\tau_{\text{cb}}^{\alpha}$ play important roles in the dislocation dissociation and slip on the octahedral slip systems, and contribute to their slip resistances. However, this is not the case for cube-slip systems, for which there are no dislocation core effects and hence the non-Schmid terms are not necessary.

Consequently, the APB shearing criterion can be formulated for two categories, viz. (i) to incorporate the non-Schmid effects in octahedral slip systems and (ii) to account for the cube-slip systems. To accommodate these phenomena in the crystal plasticity formulation, the APB shearing criterion in [23] is extended as follows:

$$\tau_{\text{eff}}^{\alpha} = \left|\tau^{\alpha}\right| - \tau_{\text{pass}}^{\alpha} > \tau_{\text{c}} \tag{10}$$

where

$$\tau_{\text{eff}}^{\alpha} = \begin{cases} \left|\tau^{\alpha}\right| - \tau_{\text{pass}}^{\alpha} & \text{for} \left|\tau^{\alpha}\right| > \tau_{\text{pass}}^{\alpha} \\ 0 & \text{for} \left|\tau^{\alpha}\right| \le \tau_{\text{pass}}^{\alpha} \end{cases} \tag{11}$$

The critical shear stress τ_{c} in Equation (10) for octahedral slip systems is a function of the primary and secondary shear stresses on the octahedral planes, shear stress on the cube plane, temperature and the APB energy on the octahedral and cube planes. For the cube-slip systems τ_{c} is just a function of temperature. Correspondingly, these dependencies are stated as:

$$\tau_{\text{c}}^{\alpha} = \left\{ \begin{array}{ll} \tau_{\text{co}}^{\alpha} = \tau_{\text{co}}^{\alpha}\left(\tau_{\text{pe}}^{\alpha}, \tau_{\text{se}}^{\alpha}, \tau_{\text{cb}}^{\alpha}, \theta, \Gamma_{1\,1\,1}, \Gamma_{0\,1\,0}\right) & \text{on octahedral slip systems} \\ \\ \tau_{\text{cc}} = \tau_{\text{cc}}(\theta) & \text{on cube-slip systems} \end{array} \right\} \tag{12}$$

Furthermore, the critical shear stress for octahedral slip systems in Equation (12) can be expressed as a function of the dislocation density due to cross-slip, i.e.

$$\tau_{\text{co}}^{\alpha} = \xi\mu\sqrt{\rho_{\text{CSD}}^{\alpha}} \qquad \text{for octahedral slip systems} \tag{13}$$

where μ is the shear modulus defined in [10]. The temperature parameter ξ accounts for the strength of the pinning obstacles. This strength decreases with increasing temperature, according to an exponential relation given in [10] as:

$$\xi = \xi_0 \exp\left(\frac{A}{\theta - \theta_c}\right) \tag{14}$$

where ξ_0 and A are materials constants θ is absolute temperature, and θ_c is a critical temperature that can be approximated as the precipitation temperature for γ' particles [10]. The dislocation density $\rho_{\text{CSD}}^{\alpha}$ due to cross-slip is given in [10] as:

$$\rho_{\text{CSD}}^{\alpha} = \rho_0 \exp\left(-\frac{H^{\alpha}}{K_{\text{B}}\theta}\right) \tag{15}$$

where ρ_0 is the dislocation density due to cross-slip at overall yield and H^{α} is the activation enthalpy for cross-slip. The enthalpy depends on the APB energy on the primary and secondary slip planes and the cube cross-slip plane, as well as on the resolved shear stresses acting on these planes. In [7,8] this enthalpy has been shown to be constituted of three parts given as:

$$H^{\alpha} = c_H \left\{ h + k_1(t_{\text{pe}}^{\alpha} - k_2 t_{\text{se}}^{\alpha}) + \sqrt{\left(\frac{1}{\sqrt{3}} - \frac{\Gamma^{0\,1\,0}}{\Gamma^{111}} + \left|t_{\text{cb}}^{\alpha}\right|\right)\frac{b}{B}} \right\} \tag{16}$$

where h, k_1 and k_2 are materials constants to be calibrated, Γ^{111} and Γ^{010} (J/m^2) are the APB energies per unit area on cube and octahedral planes, respectively. The normalized slip system resolved shear stresses t_{xx}^{α} and constants B and c_H are defined in [7] as:

$$t_{xx}^{\alpha} = \frac{\tau_{xx}^{\alpha}}{\Gamma^{111}/b}, \quad B = \frac{\mu b^2}{2\pi\Gamma^{111}} \quad \text{and} \quad c_H = \frac{\mu b^3}{4\pi}$$

The cross-slip dislocation densities increase with increasing temperature, and with the formation of thermally activated constrictions. The increase in cross-slip dislocation densities results in increasing critical shear stress corresponding to Equation (13). At the same time, there is a reduction in the strength of obstacles with an increase in temperature according to Equation (14). Thus, with increasing temperature, there is a competition between increasing strength due to formation of KW locks and obstacle strength reduction. The model can be used for the matrix-precipitate APB shear modelling in Ni-based superalloys.

4. Calibration and validation of the proposed model

The model developed in Section 3 is calibrated and validated in this section for variants of single crystals Ni$_3$Al. A crystal plasticity finite element model implementing Equations ((4)–(16)), similar to [22,23], is developed for this purpose. The parameter calibration process is performed for Ni$_3$Al + 0.2%B. It is shown that most of these calibrated parameters can be applied to variants of Ni$_3$Al with minor changes. The constitutive model with hardening due to SSDs and CSDs does not contain any size dependent parameter and the results are as such not mesh sensitive. Validation of the model is done with loading corresponding to constant strain-rate and creep tests. For the creep simulations, the material is single crystal of Ni$_3$Al + 1%Ta.

4.1. *Calibrating constitutive parameters*

Constitutive parameters in the crystal plasticity model in Equations ((4)–(16)) can be divided into two categories. Parameters in the first category are taken directly from papers [8,10] found in the literature. They include h, Γ^{010}, Γ^{111}, b, μ and ρ_0, which have values 0.3, 0.083, 0.3, 2.49×10^{-10} m 142.2 GPa, and 5.0×10^{15} m/m^3, respectively. The initial value of the SSD density is obtained from the experimental data in [10] as a function of temperature given as:

$$\rho_{SSD0} = \begin{cases} 7.5 \times 10^9 - 8.36 \times 10^6\,\theta & \forall\ \theta \le 659K \\ 2 \times 10^9 & \text{otherwise} \end{cases}$$

The critical shear stress for cube-slip systems is also a parameter that belongs to this category. It varies with temperature due to creation of cross-slip just for the octahedral slip systems. From the data in [10], the cube-slip resistance is derived as:

$$\tau_{cc} = \begin{cases} 330\,\text{MPa} & \forall\ \theta \le 915K \\ 858 - 0.5777\theta\,\text{MPa} & \text{otherwise} \end{cases}$$

The remaining parameters in the constitutive model, corresponding to the second category, are calibrated from experimental data on single crystal Ni$_3$Al + 0.2%B in [25].

The parameters correspond to the yield state, temperature state and hardening state. The experiments have been conducted with an applied strain-rate loading of $\dot{\varepsilon} = \pm 1.3 \times 10^{-3} \mathrm{s}^{-1}$ for different lattice orientations, and at temperatures ranging from room temperature to 1300 K. For the calibration process, a single-crystal CPFE model is developed and simulated for various loading cases. Stress–strain plots are generated from these simulations.

4.1.1. *Constitutive parameters for the yield state*

The yield state includes yields strengths from the beginning of plastic deformation to that at 0.2% offset strain. Some of the constitutive parameters in Section 3 have more impact on this state. The parameters may be itemized as: (i) velocity of plastic shear strain in Equation (4), (ii) passing and cutting stresses in Equation (5) for the onset of plastic shear deformation and (iii) enthalpy term in Equation (16) for the yield strength corresponding to 0.2% offset strain. While these equations have multiple parameters, the important ones that are more sensitive to the yield state are listed in Table 2. The exponent p in Equation (4) is responsible for the rate of transition from elastic to the plastic state. To understand the sensitivity to p, three simulations are conducted for the [0 0 1] orientation at 1000 K for three values of p, viz. 0.5, 0.75 and 1.0. Results are shown in Figure 6. The magnitude of the yield stress is not important in this study because it can be matched by changing the other constants. The main difference among the three plots is the rate of transition from elastic to plastic state. It is clear that with increasing p this transition gets sharper. As a result, there will not be any change in yield stress for offset strains 0.05–1%. This has been reported in the literature [12,26].

The second property that is sensitive to the yield state is the activation energy Q, which exponentially changes the rates of plastic shear deformation in Equation (4). Smaller activation energy accumulates more plastic deformation at a given temperature. This results in a larger evolution of mobile dislocation densities. Higher activation energy increases the barrier strength and the velocity of dislocation drops rapidly due to exponential relation between activation energy with dislocation velocity. Three simulations for the [0 0 1] orientation at 1000 K for three activation energies $Q = 1.1 \times 10^{-20}$, 1.1×10^{-20} and 1.1×10^{-21} J respectively are performed to demonstrate the effect of activation energy on the yield state. Results are shown in Figure 7. Larger values of Q result in very small values for velocity. For activation energy of 1.1×10^{-19} J, the plastic deformation is very small and almost zero for total strain of 0.013. Higher accumulation of plastic deformation occurs by decreasing the activation energy.

Two constants k_1 and k_2 are responsible for tension–compression asymmetry in the yield state. Simulations are performed for three sets of k_1 and k_2. The values of k_1 and k_2 are 0 and 0.2, 0.5 and 0, and 0.5 and 0.2 respectively, for the first, second and third sets. The variation of the yield stress for a 0.2% offset strain as a function of temperature for the first set are shown in Figure 8 for three orientations corresponding to the

Table 2. Experimentally calibrated parameters for the yield state of the constitutive model.

Parameter	p	Q	k_1	k_2
Value	0.5	1.1×10^{-20}	0.5	0.2
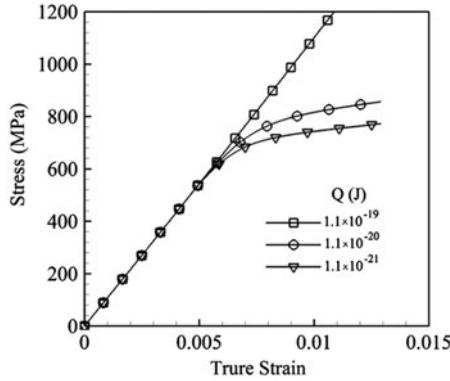
Figure 7. Sensitivity of the stress–strain response of $Ni_3Al + 0.2\%B$ single crystal to different values of activation energy Q in Equation (4).
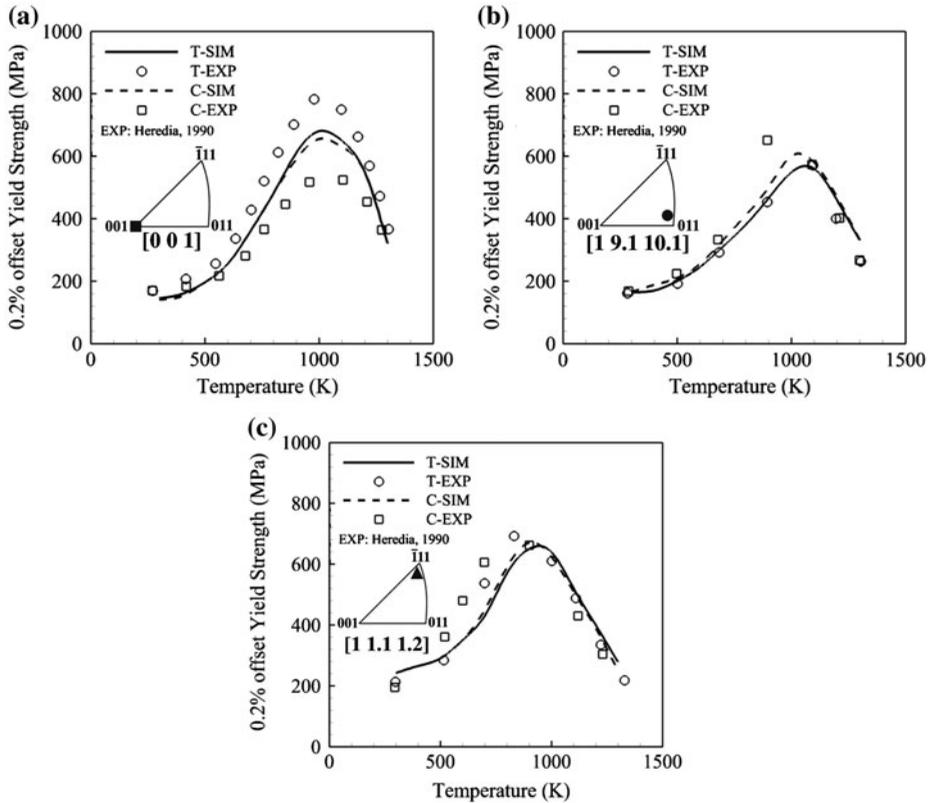
Figure 8. Variation of flow stress in $Ni_3Al + 0.2\%B$ with temperature, for different orientations in tension and compression loading: (a) [0 0 1], (b) [1 9.1 10.1], and (c) [1 1.1 1.2] for $k_1 = 0.0$ and $k_2 = 0.2$.
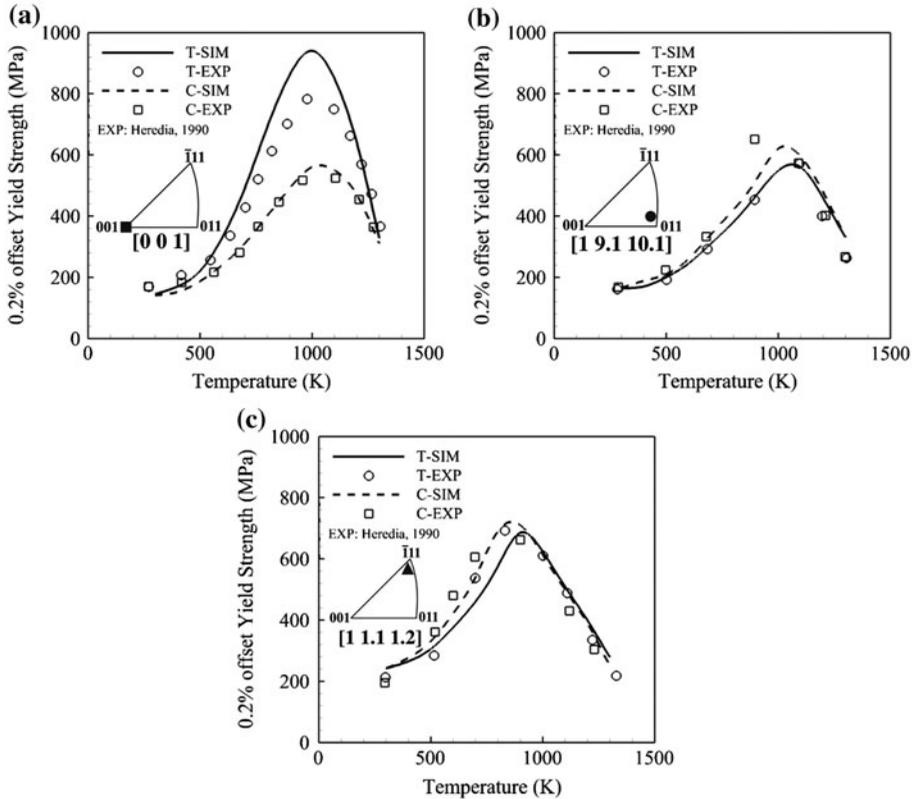
Figure 9. Variation of flow stress in $Ni_3Al + 0.2\%B$ with temperature, for different orientations in tension and compression loading: (a) [0 0 1], (b) [19.1 10.1], and (c) [1 1.1 1.2] for $k_1 = 0.5$ and $k_2 = 0.0$.

three corners of the standard unit triangle. There is slight tension–compression asymmetry around the peak temperature for orientations close to [0 0 1]. However, the asymmetry increases as it approaches the [0 1 1] orientation, and hence k_2 affects the asymmetry for orientations close to [0 1 1]. The same results are shown for the second set in Figure 9. A huge tension–compression asymmetry is seen for orientations close to [0 0 1], while it reduces closer to [0 1 1]. Results for the third set are shown in Figure 10. The enthalpy constants k_1, k_2 are obtained from results of simulations for the three orientations at 1000 K, shown in Figure 10.

4.1.2. *Constitutive parameters for the temperature state*

The second set of calibrated constitutive parameters corresponds to the temperature state and captures the anomalous behaviour of Ni_3Al alloys, given in Equation (14). The parameter ξ in this equation represents the strength of the pining obstacles and decreases with increasing temperature. The rate of this decreasing parameter increases rapidly as the upper boundary temperature θ_c is approached, at which climb mechanism
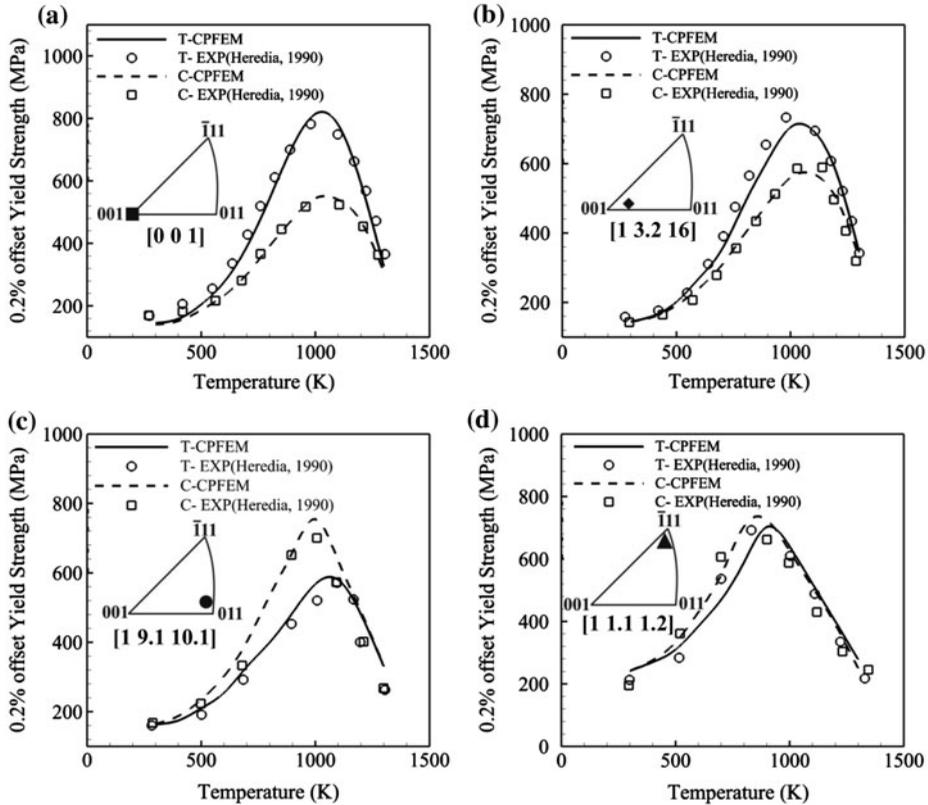
Figure 10. Variation of flow stress in $Ni_3Al + 0.2\%B$ with temperature, for different orientations in tension and compression loading: (a) [0 0 1], (b) [13.2 18], (c) [1 9.1 10.1], and (d) [1 1.1 1.2] for $k_1 = 0.5$ and $k_2 = 0.2$.

Table 3. Experimentally calibrated parameters for the temperature state of the constitutive model.

Parameter	ξ_0	A	θ_c
Value	2.1	325	1400

ensues. This parameter has a value more than unity for temperatures lower than the peak temperature and is less than unity for higher temperatures. For calibrating the three parameters ξ, A, θ_c, the yield stresses corresponding to three temperatures 300, 1000 and 1300 K for [0 0 1] orientation under tension loading are used. The calibrated parameters are listed in Table 3.

4.1.3. Constitutive parameters for the hardening state

The third set of the calibrated parameters represents the hardening state. While this is not a focus in this paper, calibrated parameters are listed in Table 4.

Table 4. Experimentally calibrated parameters for the hardening state of the constitutive model.

Parameter	c_1	c_2	c_3	c_4	c_5	c_6	c_7	c_8	c_9	c_{10}
Value	1.7×10^{16}	-3.77	4	100	1.0×10^{-3}	1.0×10^{-4}	10	10	0.3	25

4.2. *Validation of the APB Shearing Criterion*

Validation tests are performed with the CPFE model for (i) constant strain-rate loading on the alloy $Ni_3Al + 0.2\%B$ and (ii) creep loading on the alloy $Ni_3Al + 1\%Ta$.

4.2.1. *Constant strain-rate simulations*

Several orientations over the entire stereographic triangle shown in Figure 4 are selected for validation of the APB shearing model. For each orientation, tension and compression simulations are done for a set of eleven temperatures from ranging 300–1300 K at increments of 100 K. Comparison between the simulated results and experimental data are shown in Figure 10. Figure 10(a) shows the comparison for [0 0 1] orientation both in tension (*T*) and compression (*C*). The tension–compression asymmetry at low temperatures is negligible. However, significant asymmetry is observed near the peak yield stress that corresponds to temperatures in the neighbourhood of 1000 K. The peak yield stress at 1000 K is around 800 MPa in tension and less than 600 MPa in compression. At higher temperatures, this asymmetry diminishes and it tends to zero asymmetry in the high temperature ranges. The experiments show that in the stereographic triangle ([0 0 1], [0 1 1], [1 1 1]) orientations close to the [0 0 1] corner are stronger in tension. To verify this, a comparison for the [1 3.2 18] orientation that is close to [0 0 1] corner, is shown in Figure 10(b). The same trend is seen with less tension–compression asymmetry for this orientation. However, the trend changes for the [1 9.1 10.1] orientation, which is very close to the [0 1 1] orientation. The results for this orientation are shown in Figure 10(c), where the yield stress in compression is higher than in tension. This difference is small at room temperature, but increases with the temperature increasing to a critical value T_p where the stress peak is reached, and subsequently decreases. For higher temperatures (>1100 K), the low asymmetry due to activation of cube-slip systems can be seen. While, the Schmid factor for cube-slip systems in this orientation is less than for octahedral slip systems, the critical resolved shear stress (CRSS) for cube-slip systems decreases dramatically with increasing temperature. Hence, for orientations close to the [0 1 1] corner, cube-slip systems dominate at temperatures higher than the critical temperature T_p of peak stress.

To understand the activation of cube-slip systems at temperatures less than the critical temperature, a comparison for the [1 1.1 1.2] orientation that is very close to the [1 1 1] corner is shown in Figure 10(d). In this scenario, the tension–compression asymmetry is minimal even at the critical temperature of around 900 K because of the activation of cube-slip systems. From results of these four orientations, one can infer that at the room temperature, the [1 1 1] orientation has the highest yield stress. Near the critical temperature of around 1000 K, orientations close to [0 0 1] have the highest yield stress in tension while highest yield stress in compression corresponds to orientations close to [0 1 1].

In [1] it has been argued from experimental observations that the tension–compression asymmetry should disappear along the $[0\,1\,2] - [\bar{1}\,1\,3]$ great circle, where the non-Schmid component of τ_{pe} is zero. CPFE simulations are conducted for these two orientations both in tension and compression and results are shown in Figure 11. No tension–compression is observed, which agrees with the experimental observations in [1] for these two orientations. In [12,27] it has been reported that the anomalous behaviour of single crystal and polycrystalline Ni_3Al, in terms of magnitude, depends on the definition of yield stress. This mechanism is investigated for $Ni_3Al + 0.2\%B$ in the $[0\,0\,1]$ orientation for a tension test. Figure 12 shows the variation of yield stress with temperature for offset strains 0.05–1%. The asymmetry diminishes with decreasing offset strain.
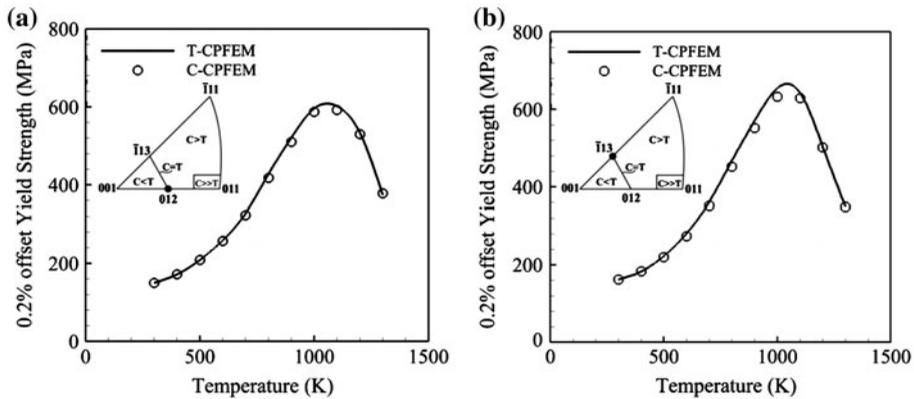
Figure 11. Variation of the flow stress with temperature for the alloy $Ni_3Al + 0.2\%B$, in tension and compression for zero tension–compression asymmetry orientations: (a) $[0\,1\,2]$, and (b) $[1\,1\,3]$.
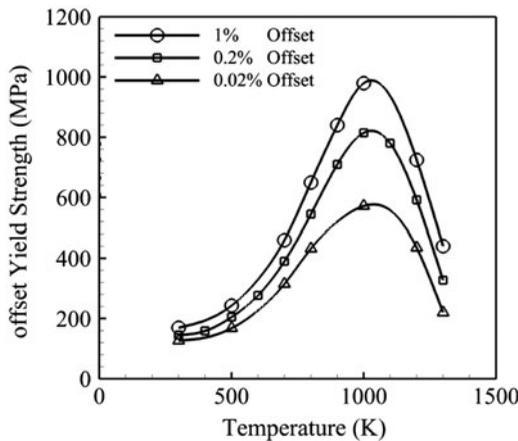
Figure 12. Variation of the flow stress with temperature for $Ni_3Al + 0.2\%B$ at different offset strains in $[0\,0\,1]$ orientation for a tension test.

4.2.2. *Creep simulations*

The same anomalies in constant strain-rate tests have been observed for creep tests. Hemker et al. [5] have studied the behaviour of single-crystal $Ni_3Al + 1\%Ta$ under creep loading conditions by surface slip trace analysis at deferent temperatures. The plastic strain corresponding to steady state creep response decreases with increasing temperature up to the critical temperature T_p and subsequently increases dramatically. Primary and secondary octahedral slip systems are activated in the primary creep stage, whereas in the secondary stage the cube cross-slip system operates [28]. In primary creep, superdislocations glide on octahedral planes consisting mainly of long and straight screws, which are in the form of KW locks. This is similar to microstructures observed in constant strain-rate tests below the critical temperature T_p, for which the octahedral slip systems have a lower CRSS than cube systems. Upon loading, slip is initiated on an octahedral plane. As the $\langle 1\,1\,0 \rangle$ super-dislocations spread out on $\{1\,1\,1\}$, their screw segments undergo cross-slip from the octahedral plane to the cube cross-slip plane, forming KW locks driven by the anisotropy of APB energy.

To validate the model for creep, CPFE simulations are carried out at an intermediate temperature for single crystal $Ni_3Al + 1\%Ta$. The constitutive parameters are calibrated from experimental data in [5] and are the same as in Table 2. However, due to change of the alloy material from Boron to Tantalum, only two parameters, viz., $\xi_0 = 1.2$ and $c_1 = 0.85 \times 10^{16}$ have been found to be different. Experimental results in Zhu et al. [28], covering three corners of the stereographic triangle at 520 °C under compression load 550 MPa are used for validation. CPFE simulations are done for the three orientations shown in the stereographic unit triangle of Figure 13. These orientations are: [1 2 3], [1 1 12] (7° away from [0 0 1]), and [11 11.5 12], (~2° off from [1 1 1]). The maximum octahedral Schmid factors for these three orientations are 0.47, 0.44 and 0.30 respectively. For the [1 2 3] and [1 1 12] orientations, the octahedral slip
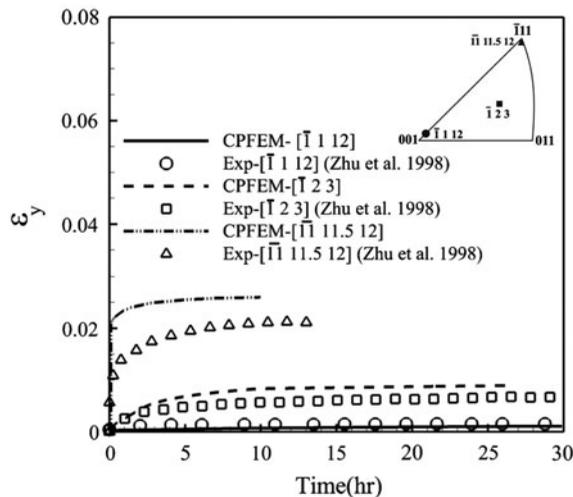
Figure 13. Creep simulations for three orientations of $Ni_3Al + 1\%Ta$ at 520 °C with compression stress of 550 MPa.

systems are activated initially that result in higher plastic strains under steady-state creep conditions. However, for the [11 11.5 12] orientation, where the maximum Schmid factor for the cube-slip system is 0.48, cube-slip systems are activated primarily and this is the reason for higher plastic strain. The progress of creep strain in the loading direction as a function of time is shown in Figure 13. The results show good agreement between simulations and experimental data in [28]. However for the [1 1 1] orientation there is a difference due to the unchanged cube-slip properties.

5. Summary

This paper successfully develops a novel dislocation density-based constitutive model for $L1_2$ Ni_3Al single crystals that is able to predict its non-conventional thermomechanical behaviour, including the anomalous temperature dependence of flow stress and hardening evolution, as well as the orientation-dependent tension–compression asymmetry. The model considers four octahedral primary and secondary slip planes corresponding to the {1 1 1} family, with three slip directions of the family $\langle 1\,1\,\bar{2} \rangle$ for each of slip plane. In addition, thermally activated cross-slip results in the activation of cube planes and non-Schmid components of the resolved shear stress. A major contribution of this work is the development of a criterion for APB shearing in the crystal plasticity model. This APB criterion is formulated to incorporate the non-Schmid terms in the flow rule for octahedral slip systems and also to account for the cube-slip systems. The critical shear stress for octahedral slip systems is a function of the primary and secondary shear stresses on the octahedral planes, shear stress on the cube plane, temperature and the APB energy of the octahedral and cube planes, while for the cube-slip systems is just a function of temperature. The model also incorporates the evolution of dislocation density due to cross-slip that depends on the APB energy of the primary and secondary slip planes and the cube cross-slip plane, as well as on the resolved shear stresses acting on these planes.

The resulting crystal plasticity model with parameters calibrated from experiments is able to capture the anomalous phenomenon of increasing flow stress with increasing temperature followed by a rapid decrease for all crystal orientations. Furthermore, the expression for activation enthalpy for cross-slip allows for adequate representation of the tension–compression asymmetry of selected slip systems. For orientations close to [0 0 1] in the unit stereographic triangle, flow stress in tension is stronger than compression, while by moving to the [0 1 1] corner it changes to compression having the higher flow strength. Orientations on the line between [0 1 2] and [1 1 3] show zero asymmetry in tension–compression. By moving to [1 1 1] corner, cube-slip systems begin to activate and asymmetry in tension–compression disappears. The value of the flow stress and its dependence on temperature depends on the composition of the particular $L1_2$ alloy being modelled. The proposed model can accommodate a variety of alloys by calibration of a few parameters as done for $Ni_3Al + 1\%Ta$ and $Ni_3Al + 0.2\%B$ in this paper with only two parameter changes.

Disclosure statement

No potential conflict of interest was reported by the authors.

Funding

References

[1] C. Lall, S. Chin and D.P. Pope, Metall. Trans. A 10 (1979) p.1323.
[2] M. Nemoto, J. Echigoya and H. Suto, Jpn. Soc. Elec. Mic. 26 (1977) p.467.
[3] P. Lours, A. Coujou and P. Coulomb, Acta Metall. Mater. 39 (1991) p.1787.
[4] P.B. Hirsch, Phil. Mag. A 65 (1992) p.569.
[5] K. Hemker, M.J. Mills and W.D. Nix, Acta Metall. 39 (1991) p.1909.
[6] S. Takeuchi and E. Kuramoto, Acta Metall. 21 (1973) p.415.
[7] V. Paidar, D.P. Pope and V. Vitek, Acta Metall. 32 (1984) p.435.
[8] A.M. Quitino and M. Ortiz, Mater. Sci. Eng. A 170 (1993) p.111.
[9] Q. Qin and J.L. Bassani, J. Mech. Phys. Solids 40 (1992) p.813.
[10] C.D. Allan, *Plasticity of nickel base single crystal superalloys,* PhD thesis, MIT 1995.
[11] T. Kameda and M.A. Zikry, Scr. Mater. 38 (1998) p.631.
[12] Y.S. Choi, D.M. Dimiduk, M.D. Uchic and T.A. Parthasarathy, Phil. Mag. 87 (2007) p.1939.
[13] V. Paidar and V. Vitek, Int. Com. 22 (2002) p.437.
[14] P. Veysseire, Adv. Phil. Metal. (1996) p.248.
[15] C.L. Fu and M.H. Yoo, Mat. Res. Soc. Symp. Proc. 81 (1989) p.133.
[16] S.M. Foiles and M.S. Daw, J. Mater. Res. 2 (1987) p.5.
[17] B.H. Kear and G.F. Wilsdorf, Trans. TMS-AIME 224 (1962) p.382.
[18] E. Schmid and W. Boas, *Plas. Cry: With Special Reference to Metals*, F. A. Hughes Co., London, 1950.
[19] C. Rentenberger and H.P. Karnthaler, Mat. Sci. Eng.: A 319–321 (2001) p.347.
[20] S. Keshavarz and S. Ghosh, Int. J. Solids Struct. 55 (2015) p.17.
[21] R.J. Asaro and J.R. Rice, J. Mech. Phys. Solids 25 (1977) p.309.
[22] S. Ghosh and S. Keshavarz, *55thAIAA/ASMe/ASCE/AHS/SC Structures, Structural Dynamics, and Materials Conference*: SciTech 2014, January 2014.
[23] S. Keshavarz and S. Ghosh, Acta Mater. 61 (2013) p.6549.
[24] T. Tinga, W.A.M. Brekelmans and M.G.D. Geers, Model. Simul. Mater. Sci. Eng. 015005 (2010) p.1.

[25] F. Roters, P. Eisenlohr, L. Hantcherli, D.D. Tjahjanto, T.R. Bieler and D. Raabe, Acta Mater. 58 (2010) p.1152.
[26] A. Arsenlis and D. Parks, J. Mech. Phys. Solids. 50 (2002) p.1979.
[27] P.H. Thornton, R.G. Davies and T.L. Johnston, Metall. Trans. 1 (1970) p.207.
[28] W.H. Zhu, D. Fort, I.P. Jones and R.E. Smallman, Acta Mater. 46 (1998) p.3873.